Nanoarchitectonics of fluorescent gold nanoclusters: A platform for image guided photodynamic therapy of hypoxic tumor

A.N Resmi, S Sivaselvam, C.R Rekha, Emilia Papasouli, Jibin Kunnumpurathu, C.S. Praveen, Emmanuel N Koukaras, Michel Rerat, Panaghiotis Karamanis, Ramapurath S Jayasree

Applied Materials Today 39 (2024) 102273

Contents lists available at ScienceDirect

Applied Materials Today

journal homepage: www.elsevier.com/locate/apmt

Nanoarchitectonics of fluorescent gold nanoclusters: A platform for image guided photodynamic therapy of hypoxic tumor

Resmi A.N. [a], Sivaselvam S. [a], Rekha C.R. [a], Emilia Papasouli [c], Jibin Kunnumpurathu [a], C.S. Praveen [d], Emmanuel N. Koukaras [b], Michel Rerat [c], Panaghiotis Karamanis [c,*], Ramapurath S. Jayasree [a,*]

[a] Division of Biophotonics and Imaging, Department of Biomaterial Sciences and Technology, Biomedical Technology Wing, Sree Chitra Tirunal Institute for Medical Sciences and Technology (SCTIMST), Trivandrum 695012, India
[b] Department of Chemistry, Laboratory of Quantum and Computational Chemistry, Aristotle University of Thessaloniki, GR 541 24, Thessaloniki, Greece
[c] CNRS/UNIV Pau & Pays Adour, Institut Des Sciences Analytiques et de Physico-Chimie pour l'environnement et les Materiaux, Hélioparc Pau Pyrénées 2avenue du Président Angot, 64000, 64053 UMR5254, Cedex 09, PAU, France
[d] International School of Photonics, Cochin University of Science and Technology, University Road, South Kalamassery, Ernakulam, Kerala 682022, India

ARTICLE INFO

Keywords:
Metal nanocluster
Cysteine gold cluster
Hypoxia
Photosensitizer
Photodynamic therapy

ABSTRACT

Metal nanoclusters are atomically precise materials comprising metal core of few atoms exhibiting unique photoluminescence properties, unlike their bigger counterparts. Some metal nanocluster with ligand-to-metal charge transfer, long-lived excited state and excited triplet state contribute to inherent photosensitizing (PS) property. However, the therapeutic efficacy of PDT is hindered by the insufficient oxygen supply (O_2) in tumor microenvironment. In the present work, cysteine-capped gold nanocluster (AuC) are studied for their unique molecular architecture for PS efficiency. The co-existence of monodispersed and self-assembled structures contribute to the photoluminescence from the quantum confinement of electronic states and aggregation-induced emission (AIE) based PS property, respectively. In-silico model was performed to study the interaction of cysteine to gold cluster, its ground and excited-state properties and the charge transfer mechanism. The AuC as PS generates cytotoxic radicals in both Type I and Type II photodynamic pathways and the dominant radical species involved were elucidated by EPR spectroscopy. *In vitro* analysis in HeLa cells showed excellent biocompatibility and bioimaging properties. The intracellular ROS production and Live/Dead assay confirmed the generation of ROS in HeLa cells upon laser irradiation. The image-guided photodynamic property with synergistic Type I and Type II PDT reactions of AuC promises its potential application in cancer therapy in both hypoxic and normoxic conditions

1. Introduction

Metal nanoclusters have received great interest in recent years due to its inherent fluorescence and unique structure comprising only few metal atoms. Significant progress has been achieved in the solution-phase synthesis of atomically precise thiolate-protected gold nanoclusters. These nanoclusters are made up of a defined number of gold atoms (n) and ligands (m) and are generally represented as $Au_nR_{m.}$ The number of gold atoms ranges from less than 10 to few hundred, resulting in cluster sizes with less than 2–3 nm in diameter [1]. Unlike nanoparticles, nanoclusters possess distinct properties characterized by a well-defined atomic size, as they exhibit more of molecular properties and are considered to bridge the gap between nanoparticles and metal atoms [2,3]. Because of the physics of its uniqueness in electrical and optical characteristics, metal nanoclusters have found extensive applications in areas such as photoelectricity, catalysis, bio-imaging and sensing applications [4–10]. The size-dependent fluorescence of these gold nanocluster ranges from visible to near-infrared, which correlates to their ultra-small size, closely approaching the Fermi wavelength of conduction electrons (approximately 0.7 nm) [11]. This leads to the quantization of energy levels, resulting in size-dependent luminescence and other molecular-like features including HOMO–LUMO electronic transitions, increased photoluminescence and intrinsic magnetism. Considering biological application, gold nanoclusters have the benefit of

* Corresponding authors.
E-mail addresses: panagiotis.karamanis@univ-pau.fr (P. Karamanis), jayasree@sctimst.ac.in (R.S. Jayasree).

https://doi.org/10.1016/j.apmt.2024.102273
Received 21 March 2024; Received in revised form 22 May 2024; Accepted 2 June 2024
Available online 8 June 2024

having a stable chemical nature and strong biocompatibility among all metal-based nanoclusters [12]. Recent developments in the synthesis have made it simpler to make water-soluble and biocompatible gold nanoclusters with a reduced size and characteristic emission wavelength. For biomedical applications, the gold nanoclusters are usually stabilized with biocompatible agents such as proteins or other biomolecules. Although the study of gold thiolate nanoclusters began around fifteen years ago, they have attracted substantial scientific attention in the last decade, owing to their excellent chemical stability and a wide variety of potential applications [13–15].

The thiolate-protected gold clusters have been extensively studied for their absorption, luminescence, chiroptical, electrical, catalytic and magnetic properties [16,17]. However, there are not many reports on the molecular architectonics of small and hydrophilic amino acid L-cysteine-capped gold clusters and its applications. Among different amino acids, L-cysteine is one of the least abundant, yet found as a highly conserved residue within functional binding sites in proteins. L-cysteine is the only one amino acid that comprises various functional groups including sulfur, carboxylic acid (SH/S, —COOH/COO) and amines (NH_2/NH_3). These functional groups can easily attach to the surface atoms of many metals. The distinct chemistry of the thiol or thiolate group of cysteine can impart functional sites with high-affinity metal binding, allowing for steady particle dispersion in both aqueous and non-aqueous conditions. Further, L-cysteine is a simple, cost-effective and solely water-soluble amino acid that is environmentally benign. So, cysteine will be an ideal template for building fluorescent gold nanoclusters without the need for any additional reducing agent [17,18]. Among the conventional synthesis methods, microwave irradiation has been a prominent technique for gold nanocluster synthesis. It provides rapid and homogenous heating, high activation energy, cost-effectiveness and provide high product yield with good repeatability [19]. Due to the sensitivity of nanoclusters to reaction conditions, the utilization of microwave irradiation during the synthesis process could potentially offer enhanced control over the molecular architectonics of gold nanoclusters, consequently leading to an improved spectrum of characteristics [20–22].

Among various phototherapies, photodynamic therapy (PDT) offers significant benefits over conventional chemotherapy and radiation as a therapeutic modality due to its non-invasive nature, excellent tumor selectivity and low side effects [23–26]. Qing Dan et al., fabricated BSA capped Au nanocluster (BSA@Au) for oxygen dependent Type II PDT [27]. Zhang et al., prepared 1,2-bis(diphenylphosphino)ethane capped gold nanocluster that showed inherent photoluminescence property with effective production of singlet oxygen radicals (Type II PDT) [28]. However, rapid proliferation of tumor cells outpaces the available oxygen (O_2) supply and leads to the formation of aberrant vascular networks, which further hinders the diffusion of O_2 supply and result in formation of hypoxic condition. Tragically, type II PDT heavily relies on the supply of O_2 for effective radical production, which ultimately hinders its potential PDT usage. To address the limitations of conventional photosensitizers, new research based not only on experimental works, but also on theoretical quantum chemical calculations are very active. They allow for the estimation of photosensitizer geometries, electronic parameters and their spectroscopic properties [29–32]. In addition, such first principle computations may also serve as a starting point for simulations of non-perturbative real-time dynamics. In recent years, several photosensitizers with unique molecular architectonics leads to aggregation-induced emission (AIE) properties have emerged, raising hopes for resolving some of the said issues [33,34].

With this background, we synthesized highly self-assembled L-cysteine capped gold nanocluster (AuC) with inherent fluorescence and PS property by simple microwave method. The prepared AuC showed high photostability, good quantum yield and a large Stokes shift (225 nm). The interaction of cysteine with gold cluster, the ground and excited state of AuC and its charge transfer mechanism were studied using in-silico approach. Further, the as-synthesized AuC was tested for reactive oxygen species (ROS) generation capability for effective PDT application. Finally, a tumor-targeting molecule, folic acid (FA) was conjugated with AuC for selective delivery of the nanocluster to the tumor cells safeguarding the normal cells. This study provides significant insight into the development of AuC with image guided-PDT option for treating both hypoxic and normoxic tumor. A figure representing the work in total with the details of material synthesis and a schematic of the application is shown in Scheme 1.

2. Experimental section

2.1. Materials

Hydrogen tetrachloroaurate(III) trihydrate (99.9 %), 3-(4,5-dimethyl-2-thiazolyl)-2,5- diphenyl-2-*H*-tetrazolium bromide (MTT), 1,3-Diphenylisobenzofuran (DPBF), 2′,7′dichlorofluorescein diacetate (DCFH-DA), Hoechst33342, 1-Ethyl-3-(3-dimethylaminopropyl) carbodiimide (EDC) and *N*-hydroxysuccinimide (NHS), tryptophan, dimethylsulfoxide (DMSO), trie-thanolamine (TEOA), isopropanol (IPA) and 1,3-diphenylisobenzofuran (DPBF) were purchased from Sigma Aldrich. L-Cysteine hydrochloride (98 %) and folic acid (FA) were purchased from Merk. The cell culture chemicals and other chemical used in this work were of analytical grade and purchased from Himedia Laboratories. Ultrapure Millipore water (Milli Q grade; 18 $M\Omega^{-cm}$) was used in all the experiments.

2.2. Synthesis of L-cysteine capped gold quantum clusters (AuC)

In this work, we report a rapid one-pot route for the synthesis of fluorescent gold nanoclusters using L-Cysteine as a reducing agent. Briefly, 10 mL of L-Cysteine (1 mg/mL) solution was added with 500 μL of $HAuCl_4$ solution (0.5 mM) under stirring. The final solution was subjected to microwave irradiation (900 W) for 60 s. The resulting AuC solution was purified by centrifugation (12,000 rpm; 15 min) to eliminate any impurities. The detailed characterization techniques used in this study are provided in the supporting information (S1).

2.3. Folic acid functionalized AuC (AuC-FA)

For functionalizing AuC with folic acid, 5 mL of AuC (2 mg/mL) was added with EDC (0.05 M) and stirred for 2 h. Following that, NHS (0.05 M) was introduced and stirred for another 1 h. Then FA (4 mM) was gently added to the above solution and allowed to stir overnight. The final solution was washed with distilled water (15,000 rpm for 15 min) and freeze-dried.

2.4. Detection of ROS

DPBF was used as a model dye to study the generation of ROS by AuC. Briefly, 50 μL of AuC (1 mg/mL) was added to 3 mL of DPBF solution and irradiated with 532 nm laser (0.3 W/cm^2) for 180 s. The reduction in DPBF absorbance was recorded at 407 nm at predetermined time intervals. Further, EPR spectroscopy (JES FA200, JEOL, Japan) was used to confirm the radicals generation using DMPO and TEMPO as radical adduct. The AuC and AuC-FA was irradiated with laser for 180 s in the presence of respective radical adduct and the sample were loaded into quartz tube and analysed.

2.5. Cell maintenance

HeLa cells were purchased from ATCC and maintained in DMEM medium with FBS (10 %) and antibiotic (1 %). The cells were allowed to proliferate in T25 flasks at 37 °C in CO_2 (5 %) incubator. Once the cells had attained 90 % confluence, they were trypsinized and sub-cultured to the appropriate kind of culture plates for experiments. For maintaining hypoxic condition, the experimental plates were placed in a specialized

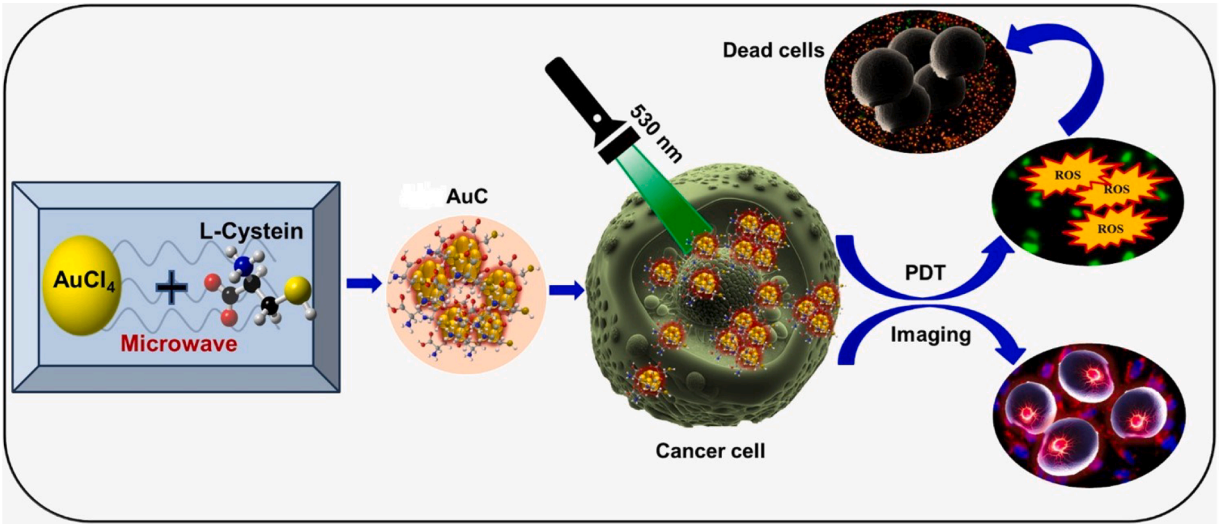

Scheme 1. Microwave synthesis of AuC using $AuCl_4$ and L-cysteine, cancer cell uptake of luminescent AuC and the working of PDT and imaging on shining a laser are depicted in this figure.

CO_2 incubator with O_2 supply of 2 %.

2.6. Cellular viability

The cell viability of AuC and AuC-FA were assessed using MTT assay as reported [35]. Briefly, HeLa cells seeded at a density of 5 x10^3 cells per well in a 96-well plate and then incubated for 24 h at 37 °C. Subsequently, the cells were exposed to AuC and AuC-FA at concentrations ranging from 20 to 200 μg/mL in a serum-free medium. After 24 h, the culture medium was replaced with 90 μL of fresh medium and 10 μL of MTT reagent (5 mg/mL) was added for 4 h incubation. Following the MTT treatment, 100 μL of DMSO was applied for 30 min and the absorbance was recorded at 570 nm using a microplate reader.

2.7. Cellular uptake and intracellular ROS generation

HeLa cells were passaged twice before being seeded at a density of 5 $\times$ 10^3 cells per well in a four-well plate. After 24 h, the cells were treated with AuC and AuC-FA (40 μg/mL) for 3 h. For the cellular uptake analysis, the cells were gently washed with PBS and imaged using a fluorescence microscope (IX51, Olympus; Japan). For the intracellular ROS production, AuC and AuC-FA treated cells were irradiated with 532 nm laser (0.3 W/cm^2) for 60 s. Finally, 1 mL of PBS containing 0.05 mM of DCFH-DA was added to each well and incubated for 30 min in dark. The cells were washed twice with PBS and imaged under a fluorescence microscope.

2.8. Live/dead assay

HeLa cells were seeded in a 4-well plate at a concentration of 2 $\times$ 10^4 cells/well. After 24 h, the cells were treated with AuC and AuC-FA for 3 h (40 μg/mL) and irradiated with laser (532 nm laser, 0.3 W/cm^2) for 180 s. Further, the cells were added with 200 μL of Live/Dead stain (Invitrogen) according to manufactures protocol and incubated in dark for 20 min. The stains were gently removed and the cells were washed twice using PBS buffer and imaged under fluorescence microscope.

2.9. Computational details

All the density functional theory calculations presented in this work are performed using the Gaussian16 package [36]. Geometry optimizations and vibrational frequency calculations for all structures were performed with the PBE0/def2SVP method using tight convergence criteria without imposing any symmetry constraints. The optical properties of the most stable structures and the geometry optimization of the singlet and triplet excited states were computed within the time-dependent density functional framework (TD-DFT) method by employing two different functionals, CAM-B3LYP [37] and PBE0 [38] respectively, using the def2SVP-PP basis set comprising relativistic corrected pseudopotentials for the treatment of the core orbitals of Au [39]. Finally, the charge transfer interactions were calculated using the CAM-B3LYP hybrid exchange-correlation functional. This functional combines the features of B3LYP with long-range correction, which adjusts the balance between short-range and long-range exchange interactions by gradually incorporating exact Hartree–Fock exchange at longer distances. CAM-B3LYP has been designed to provide more accurate predictions of excitation energies and UV–vis spectra, especially for charge-transfer states and systems with significant long-range interactions.

3. Results and discussion

3.1. Design of cysteine gold nanocluster (AuC)

The development of facile cysteine gold nanocluster (AuC) was carried out using a simple one-pot microwave synthesis. Highly fluorescent AuC was prepared using L-cysteine, which act as both ligand and reducing agent. L-cysteine exhibits high affinity for gold ions and acts as an energy-capturing antenna for luminescent centre. The HR-TEM analysis of AuC showed self-assembled architectonics with monodispersed clusters (Fig. 1a and b). The proximity and arrangement of nanoclusters within the self-assembled structures can lead to intercluster coupling which could influence the optical and electrical properties of synthesized AuC [40,41]. The schematic representation of the self-assembled architecture of AuC is depicted in Fig. 1c. The mean particle size of the prepared AuC was 3 nm. In the UV–visible spectrum, AuC exhibited a prominent absorption peak at 385 nm (Fig. 1d). The colloidal AuC was stable for more than six months and the optical characteristics did not change over this period (Fig. S1). This level of colloidal stability is very much advantageous for biological applications. Homogenous dissemination of Au, S, O, N and C was clear from the elemental mapping analysis (Fig. S2). The FTIR spectrum of L-cysteine shows characteristic peaks at 2549, 1580 and 1530 cm^{-1} which are assigned to the stretching band of —SH, asymmetric stretching band of COO— and bending vibrations of —NH respectively (Fig. 1e). The FTIR peaks of cysteine in the AuC showed a minor shift due to the change in

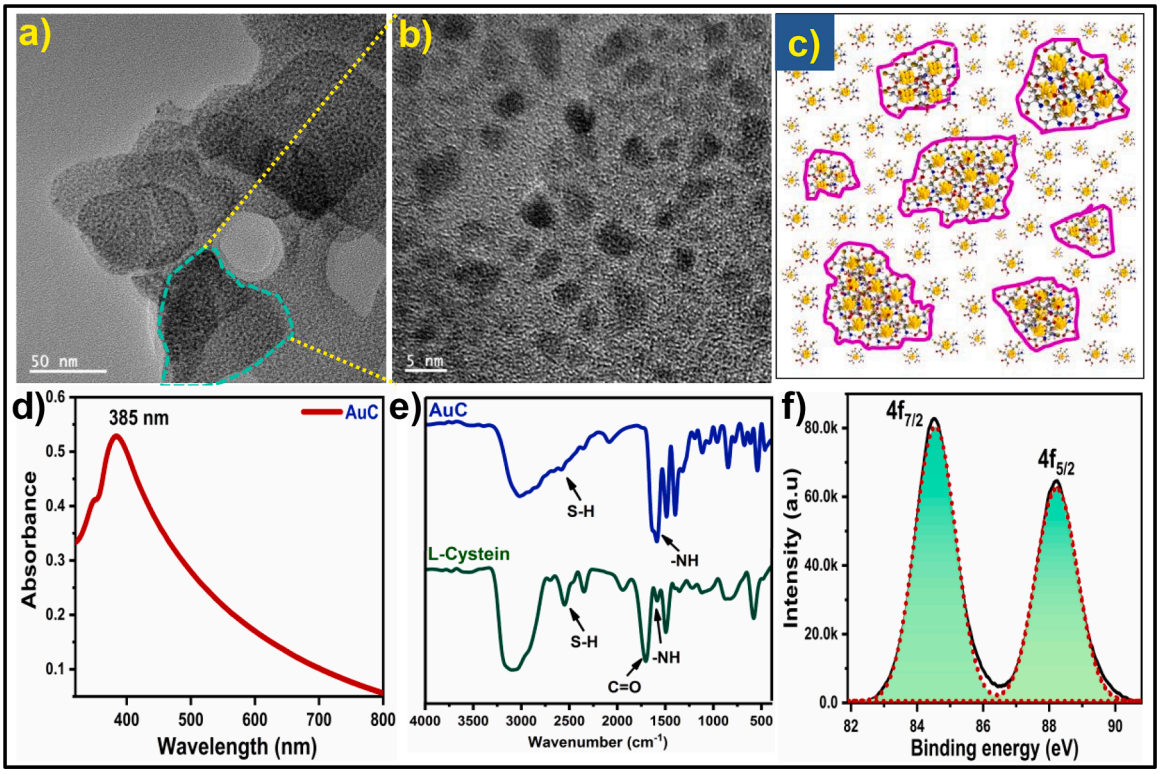

Fig. 1. Physico-chemical characterization of AuC. a) HR-TEM image of the self-assembled AuC, b) Higher magnification image of the AuC. c) Scheme representing the nanoarchitectonics of AuC in the self-assembled structures. d) UV-visible absorption spectrum of AuC. e) FTIR spectra of L-Cysteine and AuC and f) XPS spectral data of Au 4f of AuC.

the dipole moment of cysteine conjugated onto metallic nanoclusters. Moreover, the diminished intensity of the characteristic thiol (—SH) peak of L-Cysteine (2549 cm^{-1}) in the FTIR spectrum of AuC confirms the binding of L-Cysteine with gold (Au—S bond). MALDI-MS analysis was used to gain a better understanding of aspects such as ionization of the cluster and the quantification of atoms and ligands present within the nanocluster. The optical characteristics of the cluster are influenced by the number of core atoms and ligands. Based on the prior observations on the emission and absorption, the AuC of this study is assigned to have 13 core gold atoms [42,43]. Corresponding to the assigned core atoms, the number of ligands was calculated as 4 from the MALDI spectra (Fig. S3). In accordance with the analysis, the cluster composition was estimated to be $[Au_{13}(L\text{-}Cys)_4]$. Further, the oxidation states and chemical interactions between L-Cysteine and metallic gold were investigated using X-ray photoelectron spectroscopy (XPS) as illustrated in Fig. 1f. The peak of Au 4f has been resolved into spin-orbit components. The observed binding energies (BE) of the Au $4f_{7/2}$ and $4f_{5/2}$ at 84.5 and 88.2 eV respectively, fall between the BE of Au (0) of a metallic gold (84 eV) and Au (I) of gold thiolate (85 eV). From this result, we assume that both Au (0) and Au (I) coexist in AuC. The binding energy gap of 3.7 eV between these two peaks indicates that AuC has been trapped within the framework of L-Cysteine [44,45]. Comprehensive analysis of Au $4f_{7/2}$ revealed that the photoemission phenomenon depends on core and surface atoms. Negishi et al., observed that the peak position representing the inner Au was shifted monotonically from 84.0 to 84.3 eV with the reduction in core size, thereby decreasing the kinetic energy of the outgoing photoelectron (known as the "final-state effect") [45]. Conversely, the peak position of the surface Au atoms has shifted to higher energy, ranging from 84.3 to 84.7 eV. This discrepancy is attributed to an "Initial state effect" in which the electron donation occurs from the surface Au atoms to the thiolates. For the AuC of the current study, the peak position of Au $4f_{7/2}$ was at 84.5 eV, which falls within the range of 84.3–84.7 eV. Hence, it is plausible to assume that the observed chemical changes here are primarily attributable to the initial-state effect.

3.2. Fluorescence property of AuC

The AuC showed a broad emission band at 610 nm (Fig. 2a) arising from a fluorescent gold nanocluster trapped inside the framework of L-Cysteine, which is formed by the in-situ reduction of Au (III) to Au (I). The Stokes shift is as large as 225 nm, making excitation light interference minimal and allowing for photonic applications (Fig. 2b). The orange-red fluorescence of AuC was visible in various media (water, cell culture medium and saline) under UV light (365 nm) again proving its suitability for biomedical imaging (Fig. 2c). In addition, the optical emission property of AuC was analyzed using a CIE plot and power spectrum, to understand the sensitivity of fluorescence emission and color transparency of the emission. The emission observed from the cluster sample, upon excitation at 385 nm is illustrated in Fig. 2d with CIE coordinates (0.435, 0.388). The distribution of optical energy over the fluorescence spectrum is analyzed using the corresponding power spectrum (Fig. 2e). For a better understanding of the emissive state of the AuC, the emission decay lifetime was recorded at excitation/emission wavelength of 344 and 610 nm respectively. Photoluminescence lifetime was found as 0.16 μs (Fig. 2f and Table S1). This decay is in accordance with the emission mechanism involving charge transfer from the ligand to the metal nanoparticle [46]. Additionally, the Quantum yield (QY) of AuC was determined to be 7.2 % when compared to Rhodamine 6G (QY: 95 %) (Table S2). The prepared AuC exhibited better QY compared to many of the previously reported metal clusters used in PDT application. A comparison chart is depicted in Table S3.

3.3. Aggregation induced emission property of AuC

The peculiar architectonics formed by the gold clusters indicates the

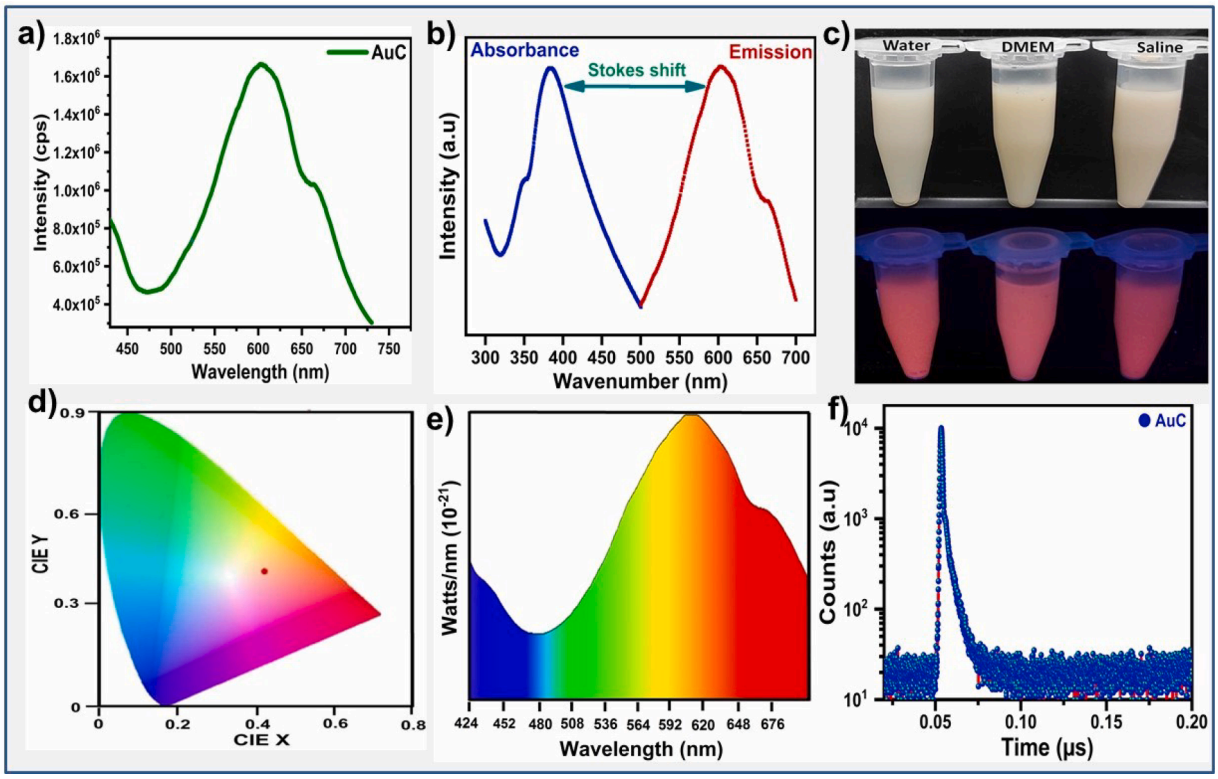

Fig. 2. Fluorescence property of AuC. a) Fluorescence spectrum of AuC, b) The stokes shift between the emission peak and the excitation peak, c) Orange-red fluorescence emission of AuC in various media under visible and UV light, d & e) represents the chromaticity diagram and the corresponding power spectrum and f) Fluorescence lifetime measurements of AuC.

possibility of self-assembly. The formation of such aggregates can be due to intermolecular interactions, which occur when molecules or particles come into proximity and interact through intermolecular forces that lead to unique nanoarchitectonics of individual units into larger structures or aggregates [47–50]. It can also be due to the solvent effect in which the properties of solvent such as polarity, hydrogen bonding and viscosity affect the intermolecular interactions that lead to the formation of self-assembled nanoarchitectonic [43,45,46,51,52]. The self-assembly of AuC depends on the aurophilic Au(I)-Au(I) interactions [42]. The exact mechanism behind aggregation-induced emission (AIE) in AuC is not yet fully understood, but it is believed to be related to the restriction of intramolecular motions or the suppression of non-radiative energy relaxation pathways upon aggregation. The close packing of the clusters is expected to limit the rotation or vibration of certain molecular segments, leading to enhanced radiative decay and higher emission intensity. To confirm the contribution of AIE, we have performed a solvent-induced aggregation study [53,54]. Initially, the emission spectrum of AuC was investigated in different water:ethanol fractions (f_w). Intense emission was observed with increased f_w without any peak shift (Fig. S4). However, the emission behaviour was not observed in 100 % ethanol. In high f_w, the AuC is expected to come closer due to intermolecular interactions resulting in larger assemblies, which can exhibit enhanced fluorescence due to AIE. To validate the observed aggregation behaviour, the absorbance of two different water:ethanol fractions (80 & 99 %) with AuC was analyzed (Fig. S5). In the visible region, a level-off tail was observed in water dominant solution, which was not the case with ethanol dominant solution. This clearly indicates the formation of aggregation and these results are in accordance with the previous reports [46,55,56]. Also, the fluorescence emission and UV–vis studies indicate that the fluorescence exhibited by the material has a contribution from the aggregation-induced emission from the controlled self-assembly of clusters in addition to the electronic transition between the $5d^{10}$ and 6 s/6p bands [45]. A number of studies have shown that a high percentage of Au(I) on the surface of thiolated AuC showed high fluorescence. The observation is in line with the reports of Luo and Goswami that Cys–Au(I) complexes on the surface of the Au(0) core can boost the cluster's PL through an aggregation-induced emission mechanism [53,56]. This observation further confirms the co-existence of Au (0) and Au(I) as seen from the XPS result.

3.4. *Photosensitising property of AuC*

Photodynamic therapy is a minimally invasive therapeutic approach for cancer treatment, utilizing light-activated photosensitizers (PSs) to generate cytotoxic free radicals (ROS). Despite its promising potential, the therapeutic efficacy of PDT is limited by the inherent challenges associated with conventional PSs thereby hindering its widespread applications. Conventional PSs were expected to have the following critical requirements: (i) The ability to absorb light within the therapeutic range (600–800 nm), ii) The high probability of intersystem spin-crossing, facilitating the efficient population of the triplet excited state, iii) Larger energy gap between the T1 and S0 states (>0.98 eV), corresponding to the energy needed to activate molecular oxygen [29]. Even though, the porphyrin based PSs satisfies the critical requirements, their clinical translation is hindered by their insoluble nature in biological media, no selectivity to tumor site and its PS effectiveness relies on oxygen atmosphere which restricts its application in hypoxic tumor. The nanoparticle has emerged as efficient PSs to overcome the limitations of conventional PSs. Hence, the photosensitizing property of AuC was investigated by evaluating its optical and electrochemical bandgap. The optical band gap of AuC from *tau* plot was calculated to be 1.15 eV (Fig. 3a). Similarly, the electrochemical bandgap was 1.56 eV and the redox potential of conduction band (E_{CB}) and valence band (E_{VB}) are determined to be −0.81 and 1.68 eV respectively (Fig. 3b). Notably, E_{CB} lies below the reduction potential (E°) of $O_2/^{\bullet}O_2^-$ (−0.16 eV), suggesting efficient energy transfer to adjacent O_2 molecule to generate reactive

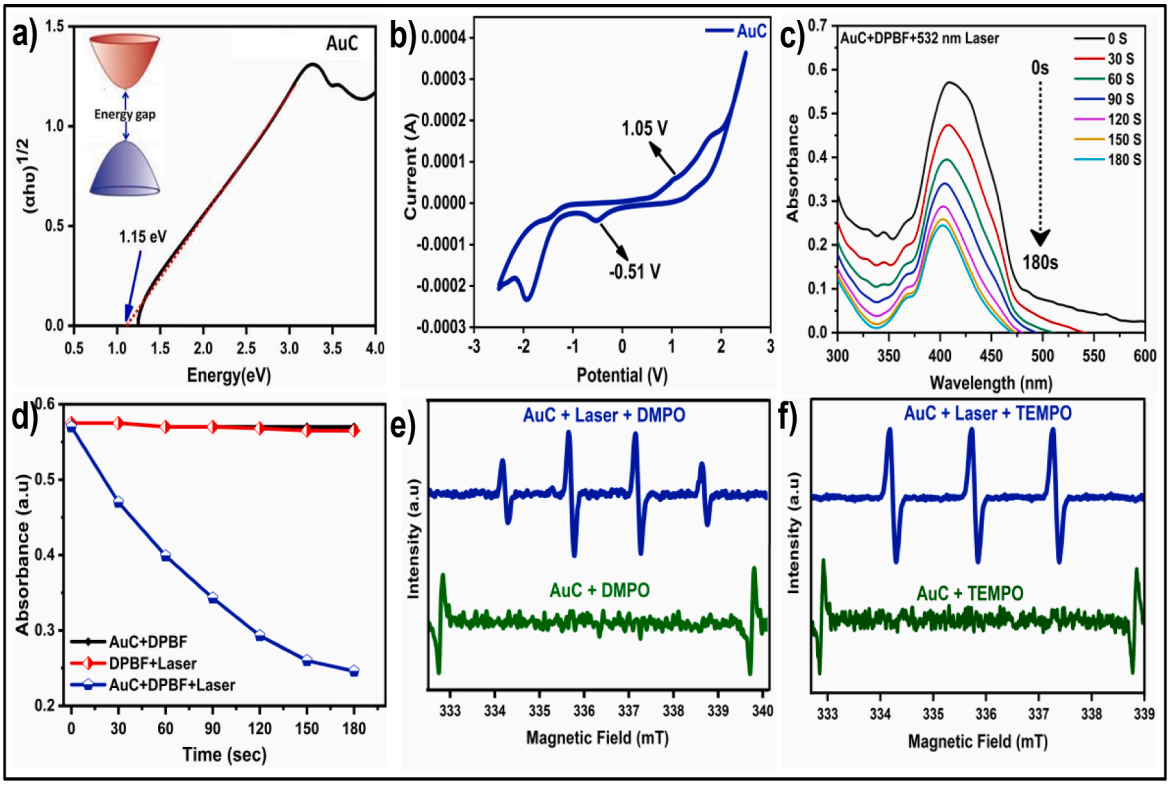

Fig. 3. Evaluation of photosensitizing property of AuC. a) Plots of $(\alpha h\upsilon)^{1/2}$ and photon energy (hυ) for the band gap energy, b) CV curve of AuC, c) Decrease in absorbance of DPBF in the presence of AuC under 532 nm laser irradiation (0.3 W/cm^2) for 180 s, d) Normalized decay curves of the DPBF absorbance at 407 nm. EPR analysis of AuC with e) DMPO and f) TEMPO as radical adduct.

oxygen species [57].

The potential of AuC for generating radical was demonstrated using a model dye DPBF. DPBF is a molecular probe used to determine the PDT efficacy and it react with singlet oxygen radical and result in reduction of DPBF intensity at 407 nm. The interaction of AuC with DPBF for 5 min exhibited no significant decrease in the absorbance, which showed the negligible role of adsorption (Fig. 3c). Similarly, laser irradiation alone showed no obvious change in the DPBF absorbance, whereas, in the presence of both AuC and laser irradiation (180 s), an obvious decrease in absorbance upto 60 % was observed (Fig. 3e and f). This result suggests the photosensitizing property of AuC. To elucidate the primary active species responsible for the degradation of DPBF, a series of radical trapping experiments were conducted by introducing specific scavengers into the system [58]. When 100 mM of triethanolamine (scavenger of h^+) and dimethylsulfoxide (scavenger of e^-) were added to the system, the degradation rate of DPBF was significantly reduced to 48 and 54 % respectively. Whereas, on addition of tryptophan (scavenger of $^1O_2$) and isopropanol (scavenger of $OH^\bullet$), the degradation of DPBF was only 20 and 8 % respectively (Fig. S6). These results suggest that the dominant reactive radical species formed in the system are a combination of singlet oxygen ($^1O_2$) and hydroxyl radical species ($OH^\bullet$). To further confirm the production of radical by AuC, EPR analysis was performed. For EPR analysis, DMPO and TEMPO are used as a radical adduct for hydroxyl and singlet oxygen radical respectively. When AuC is irradiated for 180 s in the presence of TEMPO, a characteristic three lined EPR spectra with equal intensity was observed. Similarly, in the presence of DMPO as adduct a characteristic quadrant EPR peak with 1:2:2:1 intensity was observed. The three lined and quadrant EPR spectra in the presence of TEMPO and DMPO represents the generation of $^1O_2$ and $OH^\bullet$ radical respectively, which demonstrated the contribution of AuC in both Type I and Type II PDT. The prepared AuC demonstrates significant advancements in photodynamic therapy (PDT) compared to other reported nanoclusters. [59–61]. While most previously reported metal nanoclusters primarily rely on Type II PDT mechanisms to generate singlet oxygen, the gold cluster in this study uniquely activates both Type I and Type II pathways for ROS generation.

3.5. *Computational studies*

As discussed in a previous section, the PS properties of gold clusters is related to their ability to efficiently generate triplet states once they are excited by light via intersystem spin-crossing. In the current case, this effect involves a change from a singlet state (paired-spins) to a triplet state (unpaired-spins) and it is the first crucial step for the generation reactive oxygen species under light irradiation. It is well established that the strong intersystem spin-crossing in gold clusters primarily stems from the high spin-orbit coupling inherent to gold atoms. However, there are two additional factors that could contribute to the efficient generation of high triplet populations. These are the energy gap between the singlet and triplet states and their spatial similarity. A smaller energy gap is expected to enhance the rate of inter-system-spin crossing because less energy is required for the transition. A high similarity between their spatial structures implies a high overlap between their vibrational wavefunctions. To address the latter two factors, we studied first the ground and excited state structures and properties of AuC complexes. In a next step, we performed an analysis of their excited states to check whether the presence of the L-cysteine (L-Cys) ligand is implicated in the photoexcitation processes of the crucial first singlet and triplet states of these clusters.

To accomplish the above tasks, we designed in silico more than forty initial configurations of (Au_{13}) clusters functionalized with four L-Cys molecules each in an attempt to find the most favourable binding patterns in terms of stability. Our design strategy was based on the structural results of previous studies [62] and on chemical intuition. Specifically, the initial trial systems were built upon the ground state structure of the neutral Au_{13} cluster as well as on low-lying

configurations taken from the work of Vargas et al. [62]. As far as it concerns the bonding patterns between L-Cys and gold clusters, we relied first on previous works suggesting that L-Cys primarily interacts with gold nanoparticles through its thiol groups and secondarily *via* the nitrogen and the oxygen atoms in the amino and carboxyl groups, respectively [63–66]. Here, we examined these bonding types considering also the formation of systems in which both N and S atoms bind to the surface of the cluster forming L-Cys bridges [67,68]. In addition, we assessed the interactions between L-Cys ligands.

After the geometries of all trial configurations that have been constructed as described above, they were fully optimized in the gas phase with no symmetry constrains, at the PBE0/def2SVP-PP level of theory. We concluded to twelve structurally inequivalent AuC low lying complexes in terms of energy. These configurations have been further characterized by subsequent harmonic frequency calculations to assure that they correspond to true local minima of the potential energy surface of AuC (Fig. S7). The structures of the isolated local minima confirmed that L-Cys mainly interacts with the Au cluster through its thiol group forming Au—S—Au bridges between two neighbouring Au atoms. This bonding pattern found in Au_{13} is in accord with a previous report, which studied the complexation properties of a larger gold nanocluster composed of 34 atoms [69].

Out of the final twelve low lying true local minima found in this work, we focused on the four most stable ones. The equilibrium geometries of these species and their energy differences with respect to the most stable configurations are given in Fig. 4(a). In the same figure, we also provide vertical $S_0 \rightarrow T_1$ energy differences as well as their optical gaps computed at the TD-CAM-B3LYP/def2SVP-PP level of theory on optimized geometries obtained with the same functional. A theoretical UV–vis spectrum of the four most stable configurations of AuC a complex were computed at the CAM-B3LYP/def2SVP-PP level of theory and are given in Supplementary Fig. S8. Also, we calculated the $S_0 \rightarrow T_1$ energy gaps for the two most stable configurations (0) and (1) at same level of theory. The obtained results of 1.06 and 1.03 eV are higher than the required energy gap value of 0.98 eV, which is the energy necessary to activate molecular oxygen.

To understand the charge transfer mechanism representing the $S_0 \rightarrow S_1$ and $S_0 \rightarrow T_1$ quantum transitions in the case of the most stable structures found in this work, we computed and plotted the natural transition orbitals in the case of AuC-0 and AuC-2 configurations. The respective analysis provides a compact picture about the migration of charge within a molecule during an electronic excitation [70]. As seen in Fig. 4(b), both singlet and triplet excitations are very well represented *via* a local reorganization of the electron density occurring between the molecular orbitals of the gold atoms. Also, it becomes evident that the participation of L-Cys molecules in the excitation mechanism of these species is rather limited. This is an interesting finding suggesting that the L-Cys ligands do not compromise the PS activity of the metallic core. Finally, it is revealed that both singlet and triplet states share similar density spatial distributions. This implies that both states stem from similar electronic transitions between the occupied and unoccupied complex orbitals. The same conclusion can be deducted from the rest configurations we considered in this study (Fig. S9).

In addition to the vertical excited state of the AuC complexes, we

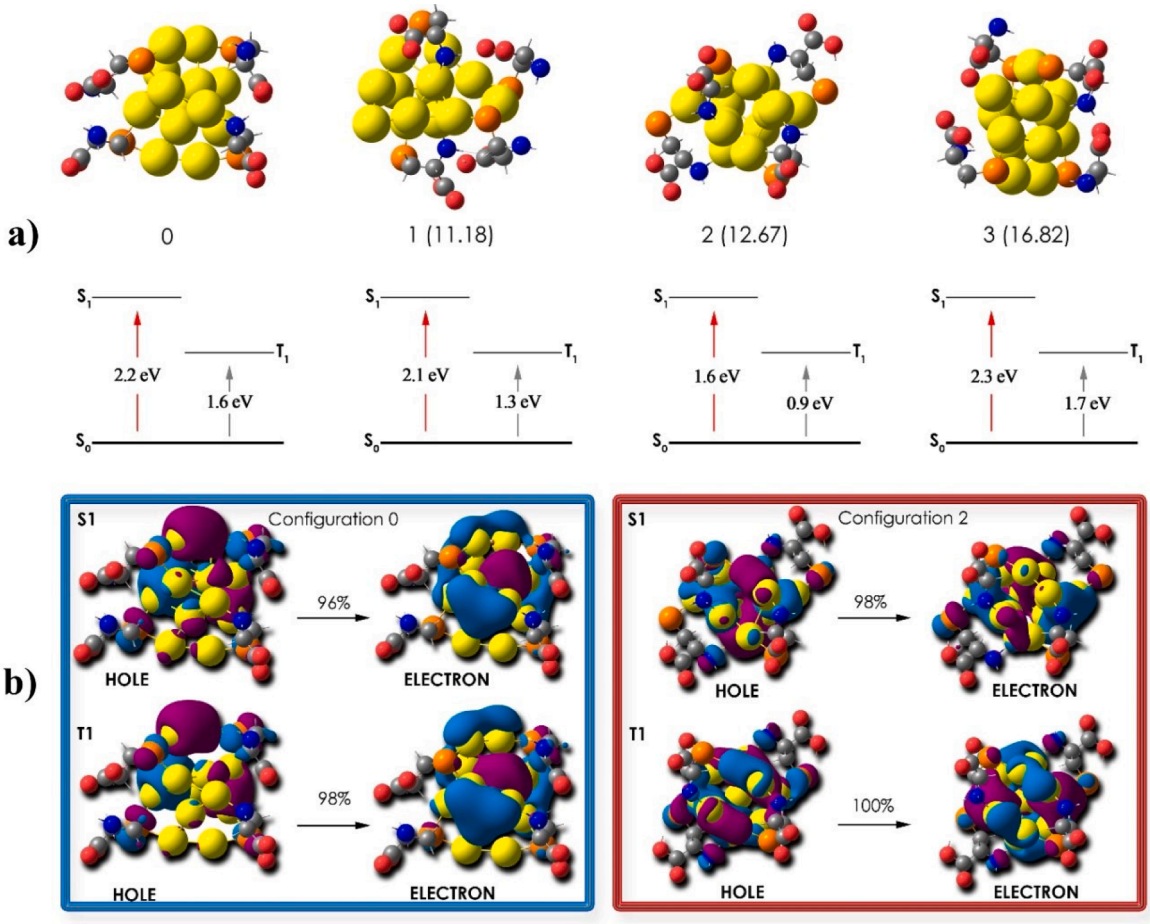

Fig. 4. a) Equilibrium geometries and excitation energies of the four most stable AuC at PBE0/def2SVP-PP level of theory, number in parentheses correspond to the relative electronic energies in kcal/mol. In all geometry optimizations Grimme's empirical dispersion (GD3) was used. The energy differences $\Delta E = E(T_1) - E(S_0)$ and $E(S_1) - E(S_0)$ have been computed with the CAM-B3LYP/def2SVP-PP method. b) Hole-electron natural transition orbitals representing the electron density reformation during the $S_0 \rightarrow S_1$ and $S_0 \rightarrow T_1$ excitations.

determined the relaxed structures the first allowed by symmetry S_1 state and those of the triplet states [71]. The results of these computations are summarized in Fig. 5 in which we compare the equilibrium nuclear geometries of the first singlet and triplet excited state of the four low-lying configurations of AuC complexes. A first glance on the visual comparisons, depicted in the form of superposed molecular structures, it becomes clear that the deviation between the equilibrium geometries of the singlet and triplet states of each of the four local minima, are significantly small. This effect is further quantified by the calculated root-mean-square differences (RMSD) values reflecting the mean interatomic distance deviation between the S_1 and T_1 equilibrium geometries. Specifically, at the respective level of theory, the obtained RMSDs vary between a rather narrow margin between 0.04 to 0.3 Å. Finally, the energy differences $\Delta E = E(T_1) - E(S_1)$ clearly point out that the singlet and triplet states of these complexes lie close in energy indicating a high probability of S_1 to T_1 intersystem crossing.

3.6. In vitro PDT efficacy

After establishing the photosensitizing property of AuC, we investigated its potential as a photodynamic therapeutic agent experimentally. Initially, a cancer-targeting agent folic acid (FA) was functionalized to AuC for selective uptake of the material to tumor *via* over expressed folate receptor in cancer cells. FTIR analysis revealed the disappearance of C═O peak in FA and the presence of intense —NH peak at 1583 cm^{-1} in AuC-FA confirms the successful functionalization of FA *via* the formation of an amide bond between its amine group and the carboxyl group of AuC (Fig. S10a). Further, the FA functionalization was confirmed by decrease in the negative zeta potential to −19 mV from −32 mV of AuC. This is due to the reduction in the carboxyl groups on the surface of AuC through the formation of amide bond with FA to form AuC-FA (Fig. S10b).

In cellular up-take analysis, the inherent fluorescent property of AuC is utilized for imaging. AuC-FA exhibited enhanced cellular uptake in cells when compared to bare AuC, due to their rapid internalization *via* receptor-mediated targeting (Fig. S11). Cell viability by MTT assays demonstrated a dose-dependent decline in HeLa cell survival after co-incubation with varying AuC and AuC-FA concentrations (20–200 μg/mL) under both normoxic and hypoxic conditions (Fig. 6a and b). However, the cell viability remained above 90 and 85 % for AuC and AuC-FA in both normoxic and hypoxic conditions respectively, which showed good cytocompatibility. The cytotoxicity analysis of AuC for 24 and 48 h also showed higher biocompatibility (Fig. S12). Further, the production of oxidative stress in cells during PDT was validated using a ROS-specific cell permeable probe 2′,7′-dichlorodihydrofluorescein diacetate (DCFH-DA). The incubation of HeLa cells with AuC and AuC-FA (normoxic) for 3 h did not result in a substantial generation of ROS compared to the control group (Fig. 6c). However, following laser irradiation (0.3 W/cm^2, 532 nm) for 60 s, a notable increase in ROS production was observed in both the treatment groups. Under hypoxic conditions, the low ROS level was observed in both AuC and AuC-FA treated cells and this could be due to the cellular stress induced by hypoxia. After laser irradiation, significant increase in ROS production was observed in both the treatment groups. A significant amount of ROS production under hypoxic condition confirms the production of hydroxyl radical (type I PDT) and the results are consistent with our EPR analysis. The elevated ROS level in AuC-FA group is due to the enhanced cellular uptake facilitated by the functionalization of AuC with folic acid followed by the PDT effect. After laser irradiation (532 nm, 0.3 W/cm^2) for 60 s, the cytotoxic analysis of AuC and AuC-FA under normoxic condition showed significant reduction in viability to 62 and 50 % respectively. Under hypoxic condition, the cell viability was further reduced to 55 and 40 % for AuC and AuC-FA respectively. These results support the potential application of AuC and AuC-FA in both type I and type II PDT (Fig. S13).

Further, Live/Dead analysis was performed in AuC and AuC-FA treated HeLa cells. In both normoxic and hypoxic conditions, control cells exhibited >95 % live cells. After laser irradiation (532 nm, 0.3 W/cm^2) for 180 s under normoxic condition, the dead cell population significantly increased in AuC treatment (Fig. 7). The number of live cells further declines in hypoxic condition of cells treated with AuC. In AuC-FA treatment group, the number of live cell was significantly reduced when compared to AuC treatment. Under hypoxic condition, nearly all the cells exhibit red colour indicating the dead cells. From these result, the inherent fluorescence and photodynamic properties of AuC has a potential to use in fluorescence imaging-assisted PDT in cancer therapy.

4. Conclusion

In summary, we synthesized a stable and biocompatible L-Cysteine stabilized gold nanocluster through a simple one-pot method. The unique nanoarchitecture exhibited by the gold cluster was thoroughly studied and demonstrated the co-existence of self-assembled and monodispersed structures. The self-assembled structures contributed to the aggregation-induced-emission and the monodispersed clusters accounted for the distinctive emission resulting from the quantum confinement of their size. Through comprehensive experimental and computational evaluation, the structure of the AuC was determined as Au_{13}(L-Cys)$_4$. The computational studies on AuC revealed that both singlet and triplet states share similar density spatial distributions. Additionally, the energy differences clearly point out that the singlet and triplet states of these complexes lie close in energy indicating a high probability of S1 to T1 intersystem crossing. The experimental studies by EPR spectroscopy confirmed the photosensitizing property of AuC *via* generation of $OH^{\bullet}$ (Type I) and $^1O_2$ (Type II) radicals. *In vitro* analysis of AuC in HeLa cells

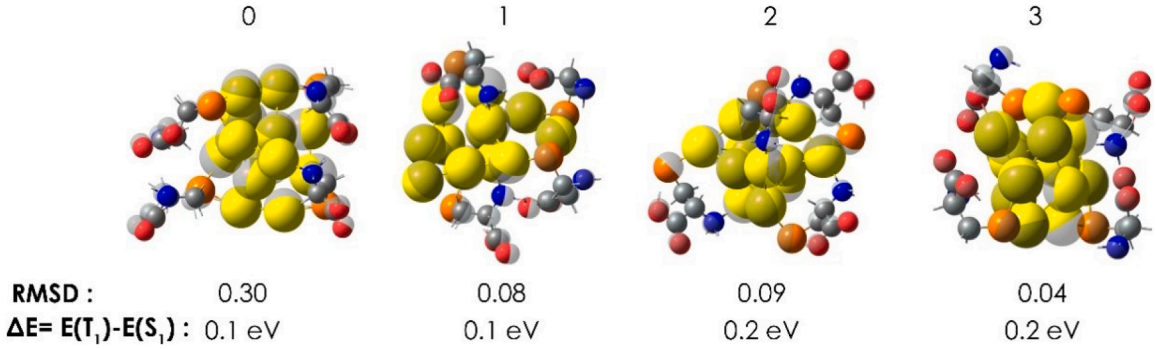

Fig. 5. Superposed equilibrium geometries, root mean square deviation of atomic position (RMSD) and energy differences ($\Delta E = E(T_1) - E(S_1)$) between S_1 and T_1 states in their equilibrium geometries. Colored atoms represent the atomic position of the clusters in their singlet and atoms in grey color correspond to the atomic position in their triplet states. All computations have been performed at the PBE0/def2SVP-PP level of theory.

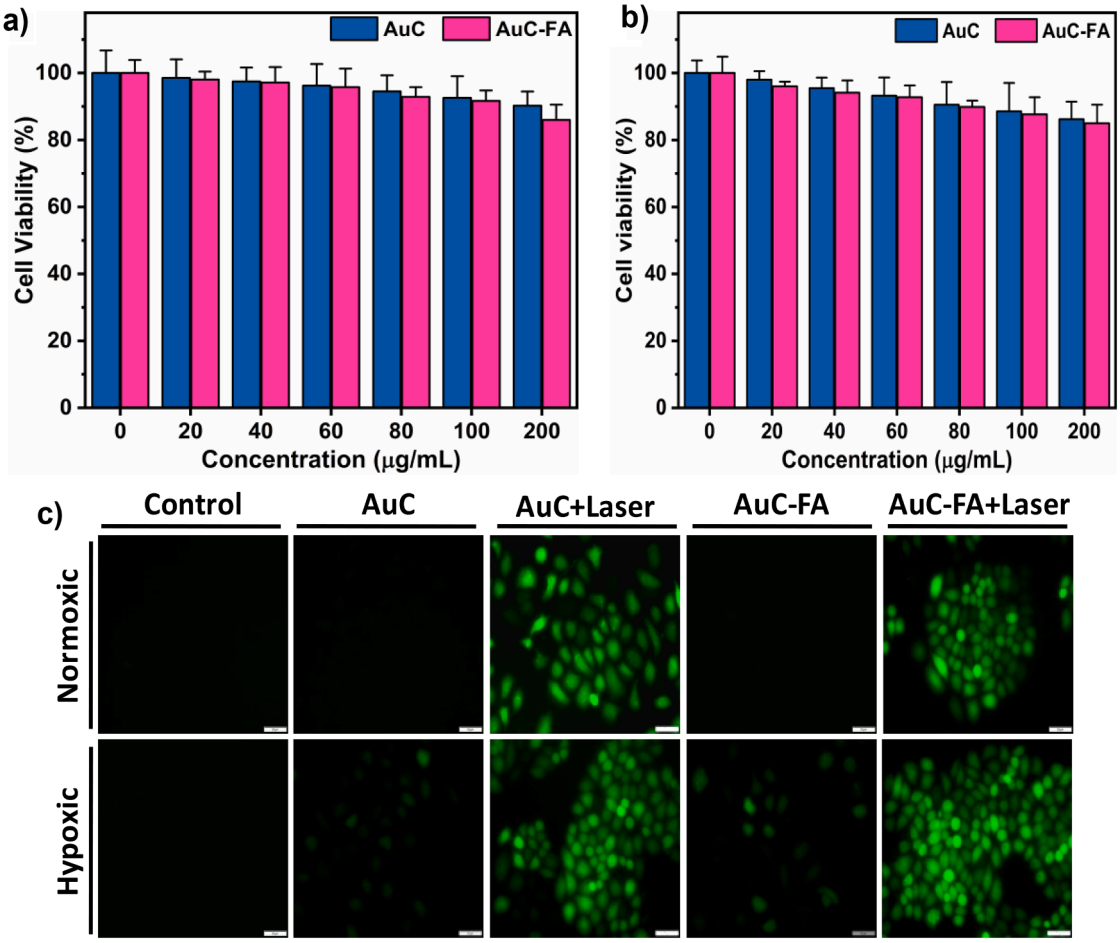

Fig. 6. Cell viability of AuC and AuC-FA on HeLa cells under a) Normoxic and b) Hypoxic condition. c) Fluorescent micrograph of ROS probe DCFH-DA in HeLa cells treated with AuC and AuC-FA (40 μg/mL). The laser power (532 nm laser) used is 0.3 W/cm^2. The error bar represents the SD of 6 independent experiments.

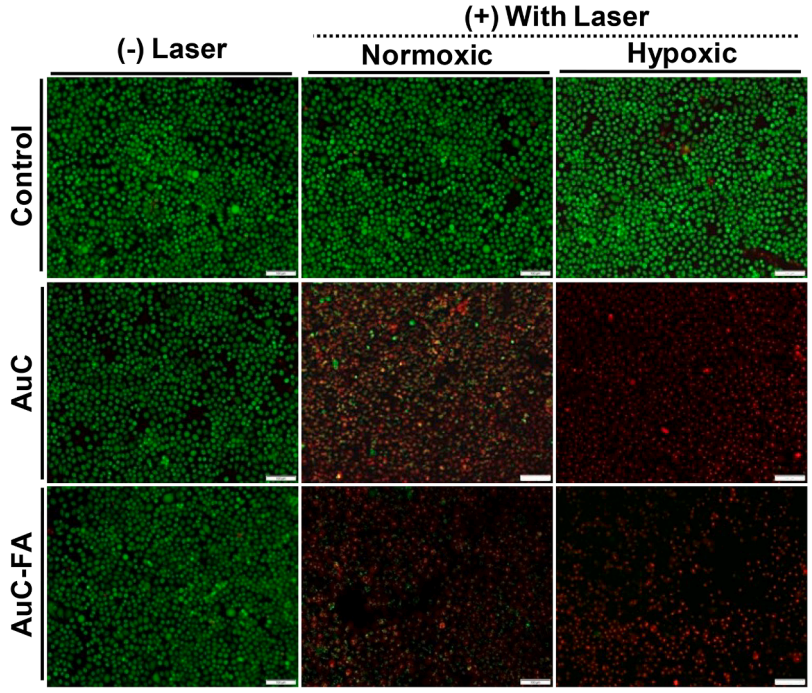

Fig. 7. Live-dead analysis of AuC and AuC-FA (40 μg/mL) with and without laser irradiation for 180 s. (All the images are taken at 100 μm scale bar).

showed good cytocompatibility. After laser irradiation, both the AuC and AuC-FA exhibited enhanced intracellular ROS generation and increased the dead cell population under both normoxic and hypoxic condition. These findings underscore the promising potential of AuC for image-guided photodynamic therapy. The combination of Type I and Type II PDT mechanisms in AuC enhances therapeutic efficacy, reduces side effects, and improves treatment outcomes. Future *in vivo* studies will explore the biodistribution and image-guided PDT capabilities of AuC in pre-clinical models. Overall, AuC holds great promise for advancing cancer theranostics by offering a powerful tool that integrates both therapeutic and diagnostic capabilities.

CRediT authorship contribution statement

Resmi A.N.: Writing – original draft, Methodology, Investigation, Conceptualization. **Sivaselvam S.:** Writing – review & editing, Writing – original draft. **Rekha C.R.:** Writing – original draft, Writing – review & editing, Investigation. **Emilia Papasouli:** Writing – review & editing, Validation, Software. **Jibin Kunnumpurathu:** Writing – review & editing, Writing – original draft. **C.S. Praveen:** Methodology, Formal analysis, Writing – review & editing. **Emmanuel N. Koukaras:** Methodology, Formal analysis, Writing – review & editing. **Michel Rerat:** Methodology, Formal analysis, Writing – review & editing. **Panaghiotis Karamanis:** Writing – review & editing, Supervision, Software. **Ramapurath S. Jayasree:** Conceptualization, Funding acquisition, Resources, Writing – review & editing, Supervision.

Declaration of competing interest

The authors declare that they have no conflict of interest.

Data availability

Data will be made available on request.

Acknowledgements

The authors R.S.J., R.A.N. and R.C.R. acknowledge Department of Biotechnology (DBT), Government of India, for the financial support of the project BT/PR27222/NNT/28/1337/2017. The author S.S acknowledges the Department of Science and Technology (DST), Science and Engineering Research Board (SERB) and the Government of India for the financial support for the N-PDF fellowship (PDF/2022/002036).

Supplementary materials

Supplementary material associated with this article can be found, in the online version, at doi:10.1016/j.apmt.2024.102273.

References

[1] G. Li, R. Jin, Atomically precise gold nanoclusters as new model catalysts, Acc. Chem. Res. 46 (2013) 1749–1758, https://doi.org/10.1021/AR300213Z/ASSET/IMAGES/MEDIUM/AR-2012-00213Z_0016.GIF.
[2] P.L. Xavier, K. Chaudhari, A. Baksi, T. Pradeep, Protein-protected luminescent noble metal quantum clusters: an emerging trend in atomic cluster nanoscience, Nano Rev. 3 (2012) 14767, https://doi.org/10.3402/NANO.V3I0.14767.
[3] M.J. Ko, W. Yoo, S. Min, Y.S. Zhang, J. Joo, H. Kang, D.H. Kim, Photonic control of image-guided ferroptosis cancer nanomedicine, Coord. Chem. Rev. 500 (2024) 215532, https://doi.org/10.1016/J.CCR.2023.215532.
[4] L.V. Nair, S.S. Nazeer, R.S. Jayasree, A. Ajayaghosh, Fluorescence imaging assisted photodynamic therapy using photosensitizer-linked gold quantum clusters, ACS Nano 9 (2015) 5825–5832, https://doi.org/10.1021/acsnano.5b00406.
[5] K. Jibin, M. Victor, G. Saranya, H. Santhakumar, V. Murali, K.K. Maiti, R. S. Jayasree, Nanohybrids of magnetically intercalated optical metamaterials for magnetic resonance/raman imaging and in situ chemodynamic/photothermal therapy, ACS Appl. Bio Mater. 4 (2021) 5742–5752, https://doi.org/10.1021/ACSABM.1C00510/SUPPL_FILE/MT1C00510_SI_001.PDF.
[6] R.V. Nair, P. Radhakrishna Pillai Suma, R.S. Jayasree, A dual signal on-off fluorescent nanosensor for the simultaneous detection of copper and creatinine, Mater. Sci. Eng. 109 (2020) 110569, https://doi.org/10.1016/j.msec.2019.110569.
[7] H. Santhakumar, R.V. Nair, D.S. Philips, S.J. Shenoy, A. Thekkuveettil, A. Ajayaghosh, R.S. Jayasree, Real time imaging and dynamics of hippocampal Zn^{2+} under epileptic condition using a ratiometric fluorescent probe, Sci. Rep. 8 (2018) 9069, https://doi.org/10.1038/s41598-018-27029-5.
[8] R.V. Nair, H. Santhakumar, R.S. Jayasree, Gold nanorods decorated with a cancer drug for multimodal imaging and therapy, Faraday Discuss. 207 (2018) 423–435, https://doi.org/10.1039/C7FD00185A.
[9] L.V. Nair, D.S. Philips, R.S. Jayasree, A. Ajayaghosh, A near-infrared fluorescent nanosensor (AuC@Urease) for the selective detection of blood urea, Small. 9 (2013) 2673–2677, https://doi.org/10.1002/smll.201300213.
[10] R.V. Nair, M.F. Puthiyaparambath, R. Chatanathodi, L.V. Nair, R.S. Jayasree, A nanoarchitecture of a gold cluster conjugated gold nanorod hybrid system and its application in fluorescence imaging and plasmonic photothermal therapy, Nanoscale 14 (2022) 13561–13569, https://doi.org/10.1039/D2NR03163A.
[11] L.V. Nair, R.V. Nair, S.J. Shenoy, A. Thekkuveettil, R.S. Jayasree, Blood brain barrier permeable gold nanocluster for targeted brain imaging and therapy: an in vitro and in vivo study, J. Mater. Chem. B 5 (2017) 8314–8321, https://doi.org/10.1039/C7TB02247F.
[12] V. Poderys, G. Jarockyte, S. Bagdonas, V. Karabanovas, R. Rotomskis, Protein-stabilized gold nanoclusters for PDT: ROS and singlet oxygen generation, J. Photochem. Photobiol. B 204 (2020) 111802, https://doi.org/10.1016/j.jphotobiol.2020.111802.
[13] Q. Yuan, Y. Wang, L. Zhao, R. Liu, F. Gao, L. Gao, X. Gao, Peptide protected gold clusters: chemical synthesis and biomedical applications, Nanoscale 8 (2016) 12095–12104, https://doi.org/10.1039/C6NR02750D.
[14] W. Kurashige, M. Yamaguchi, K. Nobusada, Y. Negishi, Ligand-induced stability of gold nanoclusters: thiolate versus selenolate, J. Phys. Chem. Lett. 3 (2012) 2649–2652, https://doi.org/10.1021/jz301191t.
[15] D. Bain, S. Maity, B. Paramanik, A. Patra, Core-size dependent fluorescent gold nanoclusters and ultrasensitive detection of Pb^{2+} ion, ACS Sustain. Chem. Eng. 6 (2018) 2334–2343, https://doi.org/10.1021/ACSSUSCHEMENG.7B03794/SUPPL_FILE/SC7B03794_SI_001.PDF.
[16] S. Knoppe, T. Burgi, Chirality in thiolate-protected gold clusters, Acc. Chem. Res. 47 (2014) 1318–1326, https://doi.org/10.1021/AR400295D.
[17] R. Jin, Quantum sized, thiolate-protected gold nanoclusters, Nanoscale 2 (2010) 343–362, https://doi.org/10.1039/B9NR00160C.
[18] G. Yang, Y. Lu, H.N. Bomba, Z. Gu, Cysteine-rich proteins for drug delivery and diagnosis, Curr. Med. Chem. 26 (2019) 1377–1388, https://doi.org/10.2174/0929867324666170920163156.
[19] F.A. Bassyouni, S.M. Abu-Bakr, M.A. Rehim, Evolution of microwave irradiation and its application in green chemistry and biosciences, Res. Chem. Intermed. 38 (2012) 283–322, https://doi.org/10.1007/S11164-011-0348-1.
[20] K. Ariga, Q. Ji, J.P. Hill, Y. Bando, M. Aono, Forming nanomaterials as layered functional structures toward materials nanoarchitectonics, NPG Asia Mater. 4 (5) (2012) e17, https://doi.org/10.1038/am.2012.30.
[21] K. Ariga, Nanoarchitectonics: the method for everything in materials science, Bull. Chem. Soc. Jpn. (2024) 97, https://doi.org/10.1093/BULCSJ/UOAD001.
[22] L. Sutrisno, K. Ariga, Pore-engineered nanoarchitectonics for cancer therapy, NPG Asia Mater. 15 (1) (2023) 1–27, https://doi.org/10.1038/s41427-023-00469-w.
[23] H.-D. Cui, D.-H. Hu, J.-N. Zhang, G.-H. Gao, C.-F. Zheng, P. Gong, X.-H. Xi, Z.-H. Sheng, L.-T. Cai, Theranostic gold cluster nanoassembly for simultaneous enhanced cancer imaging and photodynamic therapy, Chin. Chem. Lett. 28 (2017) 1391–1398, https://doi.org/10.1016/j.cclet.2016.12.038.
[24] R. Vankayala, C.L. Kuo, K. Nuthalapati, C.S. Chiang, K.C. Hwang, Nucleus-targeting gold nanoclusters for simultaneous in vivo fluorescence imaging, gene delivery, and NIR-light activated photodynamic therapy, Adv. Funct. Mater. 25 (2015) 5934–5945, https://doi.org/10.1002/ADFM.201502650.
[25] T.F. Schmidt, L. Caseli, O.N. Oliveira, R. Itri, Binding of methylene blue onto Langmuir monolayers representing cell membranes may explain its efficiency as photosensitizer in photodynamic therapy, Langmuir 31 (2015) 4205–4212, https://doi.org/10.1021/ACS.LANGMUIR.5B00166/ASSET/IMAGES/MEDIUM/LA-2015-00166Q_0010.GIF.
[26] N. Singh, R. Sen Gupta, S. Bose, A comprehensive review on singlet oxygen generation in nanomaterials and conjugated polymers for photodynamic therapy in the treatment of cancer, Nanoscale 16 (2024) 3243–3268, https://doi.org/10.1039/D3NR05801H.
[27] Q. Dan, Z. Yuan, S. Zheng, H. Ma, W. Luo, L. Zhang, N. Su, D. Hu, Z. Sheng, Y. Li, Gold nanoclusters-based nir-ii photosensitizers with catalase-like activity for boosted photodynamic therapy, Pharmaceutics. 14 (2022), https://doi.org/10.3390/PHARMACEUTICS14081645.
[28] J. Zhang, Y. Zhou, K. Zheng, H. Abroshan, D.R. Kauffman, J. Sun, G. Li, Diphosphine-induced chiral propeller arrangement of gold nanoclusters for singlet oxygen photogeneration, Nano Res. 11 (2018) 5787–5798, https://doi.org/10.1007/S12274-017-1935-2/METRICS.
[29] A. Drzewiecka-Matuszek, D. Rutkowska-Zbik, Application of TD-DFT theory to studying porphyrinoid-based photosensitizers for photodynamic therapy: a review, Molecules 26 (2021) 7176, https://doi.org/10.3390/molecules26237176.
[30] Z. Li, S. Li, Y. Guo, C. Yuan, X. Yan, K.S. Schanze, Metal-free nanoassemblies of water-soluble photosensitizer and adenosine triphosphate for efficient and precise photodynamic cancer therapy, ACS Nano 15 (2021) 4979–4988, https://doi.org/10.1021/ACSNANO.0C09913/SUPPL_FILE/NN0C09913_SI_001.PDF.

[31] R. Bardhan, S. Lal, A. Joshi, N.J. Halas, Theranostic nanoshells: from probe design to imaging and treatment of cancer, Acc. Chem. Res. 44 (2011) 936–946, https://doi.org/10.1021/AR200023X/ASSET/IMAGES/MEDIUM/AR-2011-00023X_0010.GIF.
[32] M. Kaneko, T. Nakayama, H. Seki, S. Yamamoto, T. Uemura, K. Inoue, S. Hadano, S. Watanabe, Y. Niko, Lipophilic nitrile N-oxide for catalyst-free surface modification of nanoemulsions as light-harvesting nanoantennas, Bull. Chem. Soc. Jpn. 95 (2022) 1760–1768, https://doi.org/10.1246/BCSJ.20220217.
[33] Y. Yu, H. Jia, Y. Liu, L. Zhang, G. Feng, B.Z. Tang, Recent progress in Type I aggregation-induced emission photosensitizers for photodynamic therapy, Molecules 28 (2022) 332, https://doi.org/10.3390/MOLECULES28010332, 2023.
[34] J. Dai, X. Wu, S. Ding, X. Lou, F. Xia, S. Wang, Y. Hong, Aggregation-induced emission photosensitizers: from molecular design to photodynamic therapy, J. Med. Chem. 63 (2020) 1996–2012, https://doi.org/10.1021/ACS.JMEDCHEM.9B02014/ASSET/IMAGES/LARGE/JM9B02014_0009.JPEG.
[35] S. Sivaselvam, A. Mohankumar, R. Narmadha, R. Selvakumar, P. Sundararaj, C. Viswanathan, N. Ponpandian, Effect of gamma-ray irradiated reduced graphene oxide (RGO) on environmental health: an in-vitro and in-vivo studies, Environ. Pollut. 318 (2023) 120933, https://doi.org/10.1016/j.envpol.2022.120933.
[36] Frisch, M.J.; Trucks, G.W.; Schlegel, H.B.; Scuseria, G.E.; Robb, M.A.; Cheeseman, J.R.; Scalmani, G.; Barone, V.; Petersson, G.A.; Nakatsuji, H.; et al. Gaussian 16 Rev. C.01 2016.
[37] T. Yanai, D.P. Tew, N.C. Handy, A new hybrid exchange–correlation functional using the coulomb-attenuating method (CAM-B3LYP), Chem. Phys. Lett. 393 (2004) 51–57, https://doi.org/10.1016/J.CPLETT.2004.06.011.
[38] C. Adamo, V. Barone, Toward reliable density functional methods without adjustable parameters: the PBE0 model, J. Chem. Phys. 110 (1999) 6158–6170, https://doi.org/10.1063/1.478522.
[39] D. Andrae, U. Häußermann, M. Dolg, H. Stoll, H. Preuß, Energy-adjustedab initio pseudopotentials for the second and third row transition elements, Theor. Chim. Acta 77 (2) (1990) 123–141, https://doi.org/10.1007/BF01114537.
[40] S. Kolay, D. Bain, S. Maity, A. Devi, A. Patra, R. Antoine, Self-assembled metal nanoclusters: driving forces and structural correlation with optical properties, Nanomaterials 12 (2022) 544, https://doi.org/10.3390/NANO12030544.
[41] K. Ariga, Self-assembly enabling materials nanoarchitectonics. Functional Materials from Colloidal Self-Assembly, 2022, pp. 87–107, https://doi.org/10.1002/9783527828722.CH3.
[42] H.-Y. Chang, Y.-T. Tseng, Z. Yuan, H.-L. Chou, C.-H. Chen, B.-J. Hwang, M.-C. Tsai, H.-T. Chang, C.-C. Huang, The effect of ligand–ligand interactions on the formation of photoluminescent gold nanoclusters embedded in Au(I)-thiolate supramolecules, Phys. Chem. Chem. Phys. 19 (2017) 12085–12093, https://doi.org/10.1039/C7CP01915G.
[43] Y. Negishi, T. Tsukuda, One-pot preparation of subnanometer-sized gold clusters via reduction and stabilization by meso-2,3-dimercaptosuccinic acid, J. Am. Chem. Soc. 125 (2003) 4046–4047, https://doi.org/10.1021/ja0297483.
[44] I. Russier-Antoine, F. Bertorelle, A. Kulesza, A. Soleilhac, A. Bensalah-Ledoux, S. Guy, P. Dugourd, P.F. Brevet, R. Antoine, Chiral supramolecular gold-cysteine nanoparticles: chiroptical and nonlinear optical properties, Prog. Nat. Sci. 26 (2016) 455–460, https://doi.org/10.1016/J.PNSC.2016.08.008.
[45] Y. Negishi, K. Nobusada, T. Tsukuda, Glutathione-protected gold clusters revisited: bridging the gap between gold(I)-thiolate complexes and thiolate-protected gold nanocrystals, J. Am. Chem. Soc. 127 (2005) 5261–5270, https://doi.org/10.1021/ja042218h.
[46] D.I. Krisnawati, P.-H. Hsu, Y.-H. Lin, M. Alimansur, D.S. Atmojo, E.Q. Rahmawati, D. Rahayu, M. Khafid, S.-C. Lu, T.-R. Kuo, The use of the ROS scavenger cysteine as a surface ligand of metal nanoclusters and its bactericidal elimination effect, Appl. Sci. 11 (2021) 4095, https://doi.org/10.3390/app11094095.
[47] K. Ariga, Q. Ji, M.J. McShane, Y.M. Lvov, A. Vinu, J.P.. Hill, I.norganic nanoarchitectonics for biological applications, Chem. Mater. 24 (2012) 728–737, https://doi.org/10.1021/CM202281M/ASSET/IMAGES/LARGE/CM-2011-02281M_0006.JPEG.
[48] K. Ariga, Q. Ji, W. Nakanishi, J.P. Hill, M. Aono, Nanoarchitectonics: a new materials horizon for nanotechnology, Mater. Horiz. 2 (2015) 406–413, https://doi.org/10.1039/C5MH00012B.
[49] M. Komiyama, T. Mori, K. Ariga, Molecular imprinting: materials nanoarchitectonics with molecular information, Bull. Chem. Soc. Jpn. 91 (2018) 1075–1111, https://doi.org/10.1246/BCSJ.20180084.
[50] M. Komiyama, K. Yoshimoto, M. Sisido, K. Ariga, Chemistry can make strict and fuzzy controls for bio-systems: DNA nanoarchitectonics and cell-macromolecular nanoarchitectonics, Bull. Chem. Soc. Jpn. 90 (2017) 967–1004, https://doi.org/10.1246/BCSJ.20170156.
[51] K. Ariga, Nanoarchitectonics: what's coming next after nanotechnology? Nanoscale Horiz. 6 (2021) 364–378, https://doi.org/10.1039/D0NH00680G.
[52] O. Azzaroni, K. Ariga, Nanoarchitectonics: a land of opportunities, Mater. Nanoarchitecton. (2024) 1–12, https://doi.org/10.1016/B978-0-323-99472-9.00019-5.
[53] Z. Luo, X. Yuan, Y. Yu, Q. Zhang, D.T. Leong, J.Y. Lee, J. Xie, From aggregation-induced emission of Au(I)-thiolate complexes to ultrabright Au(0)@Au(I)-thiolate core-shell nanoclusters, J. Am. Chem. Soc. 134 (2012) 16662–16670, https://doi.org/10.1021/JA306199P.
[54] Y. Jin, Q.C. Peng, S. Li, H.F. Su, P. Luo, M. Yang, X. Zhang, K. Li, S.Q. Zang, B. Z. Tang, et al., Aggregation-induced barrier to oxygen—A new AIE mechanism for metal clusters with phosphorescence, Natl. Sci. Rev. 9 (2022), https://doi.org/10.1093/NSR/NWAB216.
[55] L. Ravotto, P. Ceroni, Aggregation induced phosphorescence of metal complexes: from principles to applications, Coord. Chem. Rev. 346 (2017) 62–76, https://doi.org/10.1016/j.ccr.2017.01.006.
[56] N. Goswami, Q. Yao, Z. Luo, J. Li, T. Chen, J. Xie, Luminescent metal nanoclusters with aggregation-induced emission, J. Phys. Chem. Lett. 7 (2016) 962–975, https://doi.org/10.1021/ACS.JPCLETT.5B02765/ASSET/IMAGES/LARGE/JZ-2015-02765H_0008.JPEG.
[57] W. He, H. Jia, W.G. Wamer, Z. Zheng, P. Li, J.H. Callahan, J.J. Yin, Predicting and identifying reactive oxygen species and electrons for photocatalytic metal sulfide micro–nano structures, J. Catal. 320 (2014) 97–105, https://doi.org/10.1016/J.JCAT.2014.10.004.
[58] W. Wang, K. Xiao, L. Zhu, Y. Yin, Z. Wang, Graphene oxide supported titanium dioxide & ferroferric oxide hybrid, a magnetically separable photocatalyst with enhanced photocatalytic activity for tetracycline hydrochloride degradation, RSC Adv. 7 (2017) 21287–21297, https://doi.org/10.1039/C6RA28224E.
[59] R. Han, M. Zhao, Z. Wang, H. Liu, S. Zhu, L. Huang, Y. Wang, L. Wang, Y. Hong, Y. Sha, et al., Super-efficient in vivo two-photon photodynamic therapy with a gold nanocluster as a Type I photosensitizer, ACS Nano 14 (2020) 9532–9544, https://doi.org/10.1021/ACSNANO.9B05169/SUPPL_FILE/NN9B05169_SI_001.PDF.
[60] C. Zhang, C. Li, Y. Liu, J. Zhang, C. Bao, S. Liang, Q. Wang, Y. Yang, H. Fu, K. Wang, et al., Gold nanoclusters-based nanoprobes for simultaneous fluorescence imaging and targeted photodynamic therapy with superior penetration and retention behavior in tumors, Adv. Funct. Mater. 25 (2015) 1314–1325, https://doi.org/10.1002/ADFM.201403095.
[61] X. Wen, P. Yu, Y.R. Toh, A.C. Hsu, Y.C. Lee, J. Tang, Fluorescence dynamics in BSA-protected Au 25 nanoclusters, J. Phys. Chem. C 116 (2012) 19032–19038, https://doi.org/10.1021/JP305902W/ASSET/IMAGES/MEDIUM/JP-2012-05902W_0009.GIF.
[62] A. Vargas, G. Santarossa, M. Iannuzzi, A. Baiker, Fluxionality of gold nanoparticles investigated by born-oppenheimer molecular dynamics, Phys. Rev. B 80 (2009), https://doi.org/10.1103/PHYSREVB.80.195421.
[63] G. Dodero, L. De Michieli, O. Cavalleri, R. Rolandi, L. Oliveri, A. Daccà, R. Parodi, L-cysteine chemisorption on gold: an XPS and STM study, Colloids Surf. A 175 (2000) 121–128, https://doi.org/10.1016/S0927-7757(00)00521-5.
[64] K. Uvdal, P. Bodö, B. Liedberg, L-cysteine adsorbed on gold and copper: an X-ray photoelectron spectroscopy study, J. Colloid Interface Sci. 149 (1992) 162–173, https://doi.org/10.1016/0021-9797(92)90401-7.
[65] L. Caprile, A. Cossaro, E. Falletta, C. Della Pina, O. Cavalleri, R. Rolandi, S. Terreni, R. Ferrando, M. Rossi, L. Floreano, et al., Interaction of L-cysteine with naked gold nanoparticles supported on HOPG: a high resolution XPS investigation, Nanoscale 4 (2012) 7727–7734, https://doi.org/10.1039/C2NR32741D.
[66] H.-Y. Nie, E. Romanovskaia, V. Romanovski, J. Hedberg, Y.S. Hedberg, Detection of gold cysteine thiolate complexes on gold nanoparticles with time-of-flight secondary ion mass spectrometry, Biointerphases. (2021) 16, https://doi.org/10.1116/6.0000910.
[67] R.R. Nazmutdinov, I.R. Manyurov, T.T. Zinkicheva, J. Jang, J. Ulstrup, Cysteine adsorption on the Au(111) surface and the electron transfer in configuration of a scanning tunneling microscope: a quantum-chemical approach, Russ. J. Electrochem. 43 (2007) 328–341, https://doi.org/10.1134/S1023193507030111/METRICS.
[68] R. Di Felice, A. Selloni, E. Molinari, DFT study of cysteine adsorption on Au(111), J. Phys. Chem. B 107 (2002) 1151–1156, https://doi.org/10.1021/JP0272421.
[69] P. Rodríguez-Zamora, B. Salazar-Angeles, F. Buendía, C. Cordero-Silis, J. Fabila, L. Bazán-Díaz, L.M. Fernández-Díaz, L.O. Paz-Borbón, G. Díaz, I.L. Garzón, Revisiting the conformational adsorption of L- and D-cysteine on au nanoparticles by Raman spectroscopy, J. Raman Spectrosc. 51 (2020) 243–255, https://doi.org/10.1002/JRS.5782.
[70] R.L. Martin, Natural transition orbitals, J. Chem. Phys. 118 (2003) 4775–4777, https://doi.org/10.1063/1.1558471.
[71] O. Loboda, I. Tunell, B. Minaev, H. Ågren, Theoretical study of triplet state properties of free-base porphin, Chem. Phys. 312 (2005) 299–309, https://doi.org/10.1016/J.CHEMPHYS.2004.11.041.